


## RESEARCH ARTICLE

[View Article Online](#)  
[View Journal](#) | [View Issue](#)

 Cite this: *Inorg. Chem. Front.*, 2024, **11**, 3446

# High ratios of Ni<sup>3+</sup> and Co<sup>3+</sup> facilitated by Mn-addition for enhanced oxygen evolution reaction and ethanol oxidation reaction†

 Yi-Nuo Zhen, Ruo-Yao Fan, Xin-Yin Jiang, Ning Yu, Yong-Ming Chai\* and Bin Dong  \*

The design of dual-functional catalysts for the oxygen evolution reaction and ethanol oxidation reaction is essential for improving hydrogen production efficiency, and one of the strategies to improve catalytic performance is the incorporation of high-valence metals. However, the generation of high-valence metals has always been a challenge in the field of catalysis, and elucidating the involved mechanisms is also difficult. Herein, we synthesized a metal–organic framework (MOF) material on nickel foam (NF) using a straightforward one-step hydrothermal technique and subsequently transformed it into a metal oxide hydroxide through activation, denoted as Co<sub>1</sub>Ni<sub>0.5</sub>Mn<sub>1</sub>BDC@NF-A. The catalyst with Mn enhanced exhibits a curved sheet-like morphology, arranged in an ordered layered structure, with abundant active surfaces. Mn induces additional production of Ni<sup>3+</sup> and Co<sup>3+</sup> to accelerate the OER/EOR process. The catalyst exhibits outstanding electrochemical performance in both the OER, with an overpotential of 298 mV at 100 mA cm<sup>-2</sup>, and the EOR, with a potential of 1.30 V at 100 mA cm<sup>-2</sup>, demonstrating superior performance compared to other Ni-based and Co-based catalysts. Furthermore, to reach 100 mA cm<sup>-2</sup>, the combined EOR–HER process requires only 1.39 V, while the combined OER–HER process requires just 1.54 V. The remarkable performance is attributed to the inclusion of Mn, which can promote the transformation of morphology, mainly transforming the catalyst from disordered stacking to an ordered staggered arrangement, exposing more active sites. More importantly, XPS testing shows that Mn reduces the binding energy of the Ni/Co(II) to Ni/Co(III) transition by adjusting the hybridization effect between Ni 3d, Co 3d and O 2p orbitals, promoting the generation of Ni<sup>3+</sup> and Co<sup>3+</sup> for enhanced reaction kinetics. In summary, this work presents a simple yet effective strategy for the generation of high-valence transition metals, which can be used to accelerate the OER and EOR processes, thus offering promising prospects for advancing hydrogen production technology.

Received 10th March 2024,

Accepted 27th April 2024

DOI: 10.1039/d4qi00629a

rsc.li/frontiers-inorganic

## 1. Introduction

The growing energy demand coupled with the decline of fossil fuels has spurred efforts to explore and advance renewable and eco-friendly energy sources.<sup>1,2</sup> Over the last few decades, electrocatalytic water splitting has gained widespread recognition as a viable method for sustainable hydrogen production and addressing the global energy crisis.<sup>3–6</sup> In water splitting, the OER occurs at the anode, involving the transfer of four electrons–protons and the formation of multiple intermediates with slow kinetics. It is considered an essential step

in improving hydrogen production efficiency.<sup>7–10</sup> IrO<sub>2</sub>/RuO<sub>2</sub> is renowned for its superior activity in the OER, but its high cost, limited availability of resources, and poor stability impede its widespread industrial implementation.<sup>11,12</sup> Hence, investigating affordable and abundant non-precious-metal catalysts with high catalytic performance and exceptional stability is essential. In addition to improving hydrogen production efficiency at the catalyst level, it has been found that adding some small molecule compounds (such as glycerol, methanol and acetone) to alkaline electrolysis tanks can significantly reduce the thermodynamic potential energy of anodic oxidation reactions, thereby reducing energy consumption in the hydrogen production industry.<sup>13–15</sup> Among these compounds, ethanol stands out due to its plentiful availability, minimal toxicity, excellent safety profile and ease of handling, making it a preferred target.<sup>16,17</sup> Similar to the OER catalyst, the catalysts suitable for the ethanol oxidation reaction are platinum and Pt-based materials, which are costly and relatively low in

State Key Laboratory of Heavy Oil Processing, College of Chemistry and Chemical Engineering, China University of Petroleum (East China), Qingdao 266580, PR China. E-mail: ymchai@upc.edu.cn, dongbin@upc.edu.cn; Fax: +86-532-86981156; Tel: +86-532-86981156

† Electronic supplementary information (ESI) available. See DOI: <https://doi.org/10.1039/d4qi00629a>

durability, limiting their commercial application.<sup>18,19</sup> In this context, there is a collective effort to develop non-precious metal electrocatalysts as alternatives to Pt-based catalysts.

As a matter of fact, there have been many reports on non-precious metal catalysts for the OER or EOR individually,<sup>20–25</sup> but there are few reports on bifunctional catalysts capable of both the oxygen evolution reaction and ethanol oxidation reaction. Therefore, designing dual-functional catalysts is crucial for electrocatalytic hydrogen production. Among the most advanced non-precious metal catalysts currently available, transition metals such as Fe, Co and Ni have garnered significant attention for their exceptional performance in both the OER and EOR in alkaline media.<sup>26,27</sup> Previous studies have reported a synergistic effect between cobalt and nickel elements, which can effectively reduce the voltage required for both the OER and EOR. For instance, Shi *et al.* enhanced the OER performance with Co/N carbon nanotube catalysts by incorporating trace amounts of nickel,<sup>28</sup> and Li *et al.* designed NiCoLDH to advance research on the EOR.<sup>29</sup> Therefore, performance enhancement can be achieved through the utilization of NiCo bimetallic materials.

Currently, the activity of both the OER and EOR depends heavily on the presence of transition metal sites in high valence states.<sup>30</sup> According to reports, certain high valence metals demonstrate superior OER activity compared to their counterparts in lower valence states. For instance, the Fe<sup>4+</sup> based quadruple perovskite oxide CaCu<sub>3</sub>Fe<sub>4</sub>O<sub>12</sub> exhibits higher activity than CaFeO<sub>3</sub> containing Fe<sup>3+</sup>;<sup>31</sup> Hg<sub>2</sub>Ru<sub>2</sub>O<sub>7</sub> containing Ru<sup>5+</sup> demonstrates better OER activity than commercial RuO<sub>2</sub>.<sup>32</sup> The high valence compounds of metals play a pivotal role in both OER and EOR processes. However, the Pourbaix plot indicates that achieving complete oxidation of metals requires a higher potential. Additionally, considering Ni as an example, following the Hund rule, Ni<sup>2+</sup> with semi-filled orbitals is relatively less stable compared to high valence Ni<sup>3+</sup> and Ni<sup>4+</sup>. Simultaneously, highly oxidized metals also render oxygen unstable, predisposing it to form oxygen vacancies, potentially resulting in a reduction of the metal ions' valence state.<sup>33</sup> Therefore, while minimizing the energy required for formation and maximizing stability, dealing with highly oxidized metals poses an ideal yet challenging task.

So far, many studies have focused on constructing high-priced materials, for which heteroatom doping strategies are widely used due to their simplicity and significant effects.<sup>34,35</sup> The crucial role of Mn in promoting the high-value oxidation of metals has attracted increasing attention. For example, Gan *et al.* promoted the generation of trivalent nickel in Mn-NiFe<sub>2</sub>O<sub>4</sub> through the addition of Mn, resulting in outstanding OER performance with an overpotential of 200 mV at 50 mA cm<sup>-2</sup>.<sup>36</sup> Similarly, Fan *et al.* employed a notable CoMOF precursor (CoBDC) to synthesize trace amounts of Mn-doped cobalt spinel oxide *via* a straightforward ion exchange method at room temperature. The doping of Mn can enhance OER performance by strengthening the stability of Co–O bonds.<sup>37</sup> From this perspective, Mn has a significant promoting effect on the generation and stability of high-valence metals.

Herein, we have successfully synthesized an efficient OER/EOR electrocatalyst, named Co<sub>1</sub>Ni<sub>0.5</sub>Mn<sub>1</sub>BDC@NF-A, through hydrothermal and electrochemical activation methods. The addition of manganese induces the production of Ni<sup>3+</sup> and Co<sup>3+</sup> by adjusting the hybridization effect between the metal and oxygen. Co<sub>1</sub>Ni<sub>0.5</sub>Mn<sub>1</sub>BDC@NF-A exhibits outstanding performance in both the OER (with an overpotential of 298 mV at 100 mA cm<sup>-2</sup>) and EOR (with a potential of 1.30 V at 100 mA cm<sup>-2</sup>). This study aims to provide valuable references for the preparation of EOR and OER catalysts.

## 2. Experimental

### 2.1. Synthesis of Co<sub>1</sub>Ni<sub>0.5</sub>Mn<sub>1</sub>BDC@NF-A

Nickel foam (2 × 4 cm<sup>-2</sup>, 1.5 mm) was sonicated with 1 mol of hydrochloric acid and then with ethanol for 30 minutes. Subsequently, the cleaned NF was dried overnight in a vacuum oven at 60 °C. The preprocessed NF was then vertically immersed into a 30 mL mixed solution (24 mL DMF + 6 mL DI-water), containing 1 mmol of Co(NO<sub>3</sub>)<sub>2</sub>·6H<sub>2</sub>O, 0.5 mmol of Ni(NO<sub>3</sub>)<sub>2</sub>·6H<sub>2</sub>O, 1 mmol of MnCl<sub>2</sub>·4H<sub>2</sub>O and 1.25 mmol of terephthalic acid (BDC). The hydrothermal reaction was conducted in a 100 mL Teflon autoclave at 120 °C for 12 hours to obtain self-supported Co<sub>1</sub>Ni<sub>0.5</sub>Mn<sub>1</sub>BDC@NF. Next, the sample was washed extensively with water and ethanol and then dried under vacuum at 60 °C. After the electrochemical activation of the dried sample through CV, the final sample was successfully prepared.

### 2.2. Synthesis of Co<sub>1</sub>Ni<sub>0.5</sub>BDC@NF-A

It should be noted that the metal to ligand ratio should always be 1:1, so changing the amount of metal added will also change the amount of PTA.

Co<sub>1</sub>Ni<sub>0.5</sub>BDC@NF and Co<sub>1</sub>Ni<sub>0.5</sub>BDC@NF-A: except for not adding MnCl<sub>2</sub>·4H<sub>2</sub>O in the solution and adjusting the amount of PTA to 0.75 mmol, everything else is consistent with the synthesis of Co<sub>1</sub>Ni<sub>0.5</sub>Mn<sub>1</sub>BDC@NF and Co<sub>1</sub>Ni<sub>0.5</sub>Mn<sub>1</sub>BDC@NF-A.

### 2.3. Synthesis of Co<sub>1</sub>Mn<sub>1</sub>BDC@NF-A

Co<sub>1</sub>Mn<sub>1</sub>BDC@NF and Co<sub>1</sub>Mn<sub>1</sub>BDC@NF-A: except for not adding Ni(NO<sub>3</sub>)<sub>2</sub>·6H<sub>2</sub>O and adjusting the amount of PTA to 1 mmol, everything else is consistent with the synthesis of Co<sub>1</sub>Ni<sub>0.5</sub>Mn<sub>1</sub>BDC@NF and Co<sub>1</sub>Ni<sub>0.5</sub>Mn<sub>1</sub>BDC@NF-A.

### 2.4. Synthesis of Ni<sub>1</sub>Mn<sub>1</sub>BDC@NF-A

Ni<sub>1</sub>Mn<sub>1</sub>BDC@NF and Ni<sub>1</sub>Mn<sub>1</sub>BDC@NF-A: except for not adding Co(NO<sub>3</sub>)<sub>2</sub>·6H<sub>2</sub>O and changing the amount of PTA to 1 mmol, everything else is consistent with the synthesis of Co<sub>1</sub>Ni<sub>0.5</sub>Mn<sub>1</sub>BDC@NF and Co<sub>1</sub>Ni<sub>0.5</sub>Mn<sub>1</sub>BDC@NF-A.

## 3. Results and discussion

### 3.1. Structural characterization

The fabrication of the Co<sub>1</sub>Ni<sub>0.5</sub>Mn<sub>1</sub>BDC@NF-A material is shown in Fig. S1.† Firstly, the precursor catalyst was syn-

thesized *via* the hydrothermal method and named  $\text{Co}_1\text{Ni}_{0.5}\text{Mn}_1\text{BDC@NF}$ . Subsequently, cyclic voltammetry (CV) was employed to conduct 50 cycles of electrochemical activation on  $\text{Co}_1\text{Ni}_{0.5}\text{Mn}_1\text{BDC@NF}$ , resulting in the final catalyst, named  $\text{Co}_1\text{Ni}_{0.5}\text{Mn}_1\text{BDC@NF-A}$  (Fig. S2†).

The mechanism underlying the enhancement of the OER and EOR is illustrated in Fig. 1. The addition of Mn promotes the transformation of the structure from disorderly stacking to a layered ordered structure and the growth of tightly arranged flower-shaped microspheres, which increase the active area and enhance the reaction activity. Additionally, Mn reduces the binding energy of  $\text{Co}^{2+}/\text{Ni}^{2+}$  oxidation to  $\text{Co}^{3+}/\text{Ni}^{3+}$  by facilitating the hybridization of Co/Ni 3d and O 2p orbitals, thereby promoting the generation of  $\text{Co}^{3+}$  and  $\text{Ni}^{3+}$ . Due to the addition of Mn, more  $\text{Co}^{3+}$  and  $\text{Ni}^{3+}$  species are generated in  $\text{Co}_1\text{Ni}_{0.5}\text{Mn}_1\text{BDC@NF-A}$ , thereby accelerating the processes of oxygen evolution and ethanol oxidation reactions.

Various spectroscopic characterizations were performed to gain insight into the crystalline arrangement and chemical composition of the electrocatalysts. Initially, the primary chemical composition of  $\text{Co}_1\text{Ni}_{0.5}\text{Mn}_1\text{BDC@NF}$  was confirmed through X-ray diffraction (XRD). Before activation, as shown in Fig. 2a, three characteristic peaks at  $44.46^\circ$ ,  $51.81^\circ$  and  $73.60^\circ$  were well-assigned to metallic Ni in NF.<sup>38</sup> The strong diffraction peaks at  $17.797^\circ$ ,  $30.676^\circ$ ,  $32.713^\circ$ ,  $37.054^\circ$  and  $45.489^\circ$  were attributed to  $\text{C}_8\text{H}_6\text{Co}_2\text{O}_6$  (PDF#00-034-1897) and the peaks at  $15.699^\circ$ ,  $31.808^\circ$ ,  $35.346^\circ$ ,  $40.469^\circ$  and  $41.786^\circ$  were attributed to  $\text{C}_8\text{H}_6\text{NiO}_5\cdot\text{H}_2\text{O}$  (PDF#00-035-1677). Additionally, the peaks at  $14.053^\circ$ ,  $18.991^\circ$  and  $28.228^\circ$  indicate the successful incorporation of Mn. The above results indicate the successful synthesis of MOF structures. However, due to the influence of oxidation voltage, the composition of the MOF catalyst ( $\text{Co}_1\text{Ni}_{0.5}\text{Mn}_1\text{BDC@NF}$ ) changes. In Fig. S3,† after activation, the transformation of peaks belonging to MOFs into peaks indicative of an amorphous thin-layered structure was

observed. Research has indicated that the surface reconstruction of MOF-based electrocatalysts leads to the formation of a metal hydroxide oxide (MOOH).<sup>39</sup> Furthermore, Mn exhibits lower activity compared to Ni and Co; thus,  $\text{NiOOH}$  and  $\text{CoOOH}$  are considered the actual active substances for the OER and EOR in alkaline electrolytes.

The FT-IR spectrum (Fig. 2b) reveals prominent carboxyl vibration peaks for  $\text{Co}_1\text{Ni}_{0.5}\text{Mn}_1\text{BDC@NF}$ . Two strong carboxyl bands emerged due to the C=O vibration peak near  $1650\text{ cm}^{-1}$  and the C–O bond stretching vibration peak near  $1150\text{ cm}^{-1}$ , respectively.<sup>40</sup> Additionally,  $\text{Co}_1\text{Ni}_{0.5}\text{Mn}_1\text{BDC@NF}$  exhibited O–H stretching vibrations at  $3600\text{ cm}^{-1}$  for carboxylic acid derivatives.<sup>38</sup> More notably, a broadband existed in the region between  $1400$  and  $1600\text{ cm}^{-1}$  because of the benzene moiety in PTA.<sup>39</sup> Peaks were observed in the  $1100$ – $1000\text{ cm}^{-1}$  region because of the hydrocarbon bending vibration of the in-plane ring.<sup>39</sup> Furthermore, peaks in the range of  $850$ – $650\text{ cm}^{-1}$  were observed due to the out-of-plane C–H bending vibration. The bands at  $450\text{ cm}^{-1}$  and  $520\text{ cm}^{-1}$  typically corresponded to metal–O or metal–OH-related vibrations. These results signify the successful fabrication of MOF materials. After activation, the peak shape and position remained roughly the same as those before activation. However, there was some attenuation in the intensity of the characteristic peaks after activation, manifested by the reduction in the intensity of the O–H stretching vibration peak near  $3600\text{ cm}^{-1}$  and the significant decrease in the characterization peaks of the benzene ring structure. It is crucial to note the emergence of a prominent C=C peak around  $2200\text{ cm}^{-1}$ , suggesting partial cleavage of the benzene ring structure following activation. Various phenomena can indicate the structural transformation of terephthalic acid MOFs after activation, namely the generation of MOOH<sup>41</sup> (as observed through XRD). To investigate the role of Mn, FT-IR analysis was conducted on different samples (Fig. S4†). The FT-IR spectra of  $\text{Co}_1\text{Ni}_{0.5}\text{Mn}_1\text{BDC@NF-A}$ ,

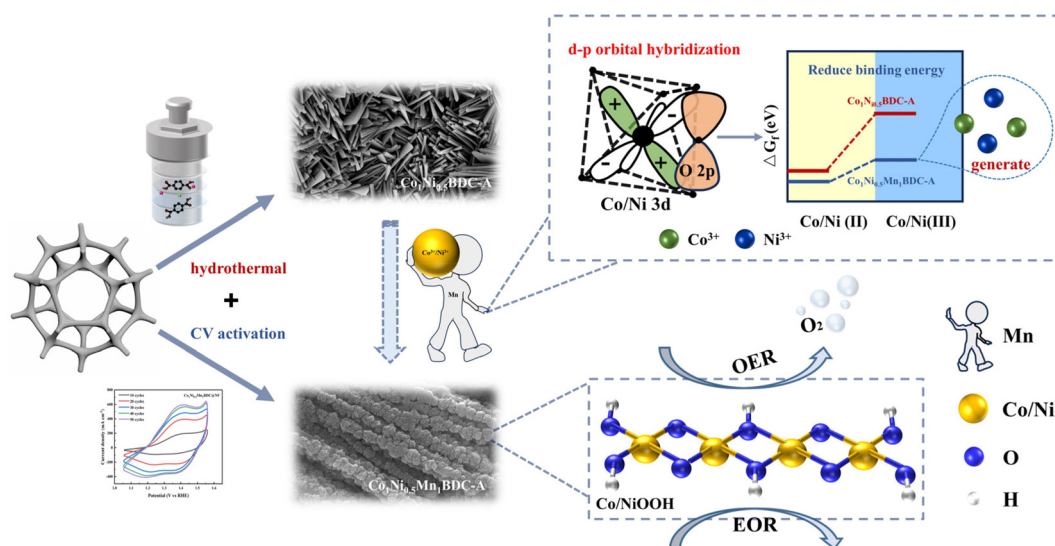


Fig. 1 Diagram illustrating the mechanism of  $\text{Co}_1\text{Ni}_{0.5}\text{Mn}_1\text{BDC@NF-A}$  in the OER and EOR.

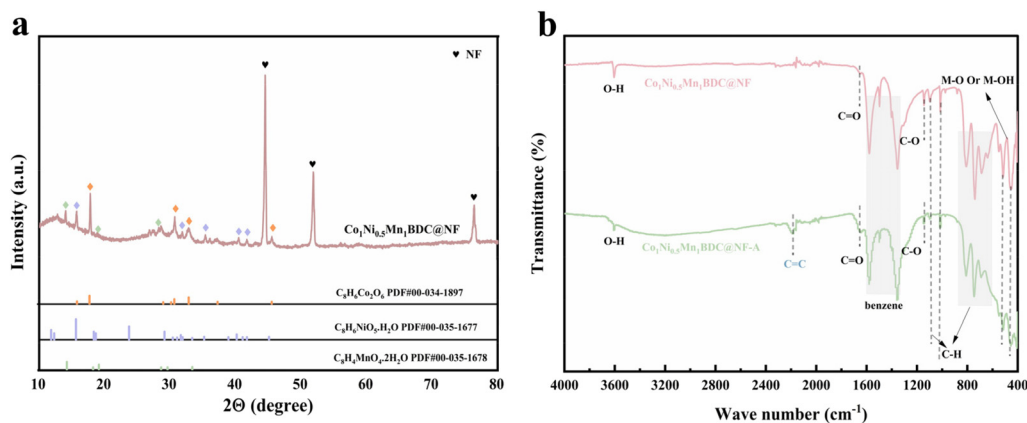


Fig. 2 (a) XRD spectrum of  $\text{Co}_1\text{Ni}_{0.5}\text{Mn}_1\text{BDC@NF}$ . (b) FT-IR spectra of  $\text{Co}_1\text{Ni}_{0.5}\text{Mn}_1\text{BDC@NF}$  and  $\text{Co}_1\text{Ni}_{0.5}\text{Mn}_1\text{BDC@NF-A}$ .

$\text{Co}_1\text{Ni}_{0.5}\text{BDC@NF-A}$ ,  $\text{Co}_1\text{Mn}_1\text{BDC@NF-A}$  and  $\text{Ni}_1\text{Mn}_1\text{BDC@NF-A}$  exhibit similar patterns, characterized by the decrease in carboxylic acid and benzene ring groups, along with the emergence of C=C bonds. Due to the almost identical peak patterns in the FT-IR spectra of different catalysts, it can be inferred that the effect of Mn addition on catalysts cannot be analyzed at the functional group level. Instead, it is inferred that Mn tends to alter the electrochemical performance by modifying the electronic structure of the metal.

The synthesized electrocatalyst's spatial morphology and elemental distribution were characterized using scanning electron microscopy (SEM) and transmission electron microscopy (TEM). As depicted in Fig. 3b and c,  $\text{Co}_1\text{Ni}_{0.5}\text{Mn}_1\text{BDC@NF-A}$  exhibits a curved sheet-like morphology and is arranged in an orderly layered structure, growing on the surface of NF. In addition, flower-shaped spheres composed of nanosheets grow

in an orderly and tightly packed manner on the sheet-like material. Due to the small volume of the spheres, while increasing the active area, they will not block the gaps between the sheets. In Fig. S5a,<sup>†</sup> it is evident that the various curved surfaces in the layered structure are not obstructed by the nanospheres. Furthermore, as shown in Fig. S5b,<sup>†</sup> the catalyst grows uniformly and ideally on the surface of NF. The advantages of  $\text{CoNiMnMOF}$  (BDC) as a precursor are as follows:<sup>42</sup> (1) the spatial confinement provided by BDC ligands enables the full dispersion and stability of active cobalt and nickel sites and (2) the presence of benzene rings in the ligand offers  $\pi$  electrons, ensuring high conductivity. As shown in Fig. 3a, the catalyst before activation ( $\text{Co}_1\text{Ni}_{0.5}\text{Mn}_1\text{BDC@NF}$ ) still exhibits a layered structure arranged in a curved sheet shape, which is conducive to providing a wider active area. However, comparing Fig. S6a and b,<sup>†</sup> it can be observed that before activation,

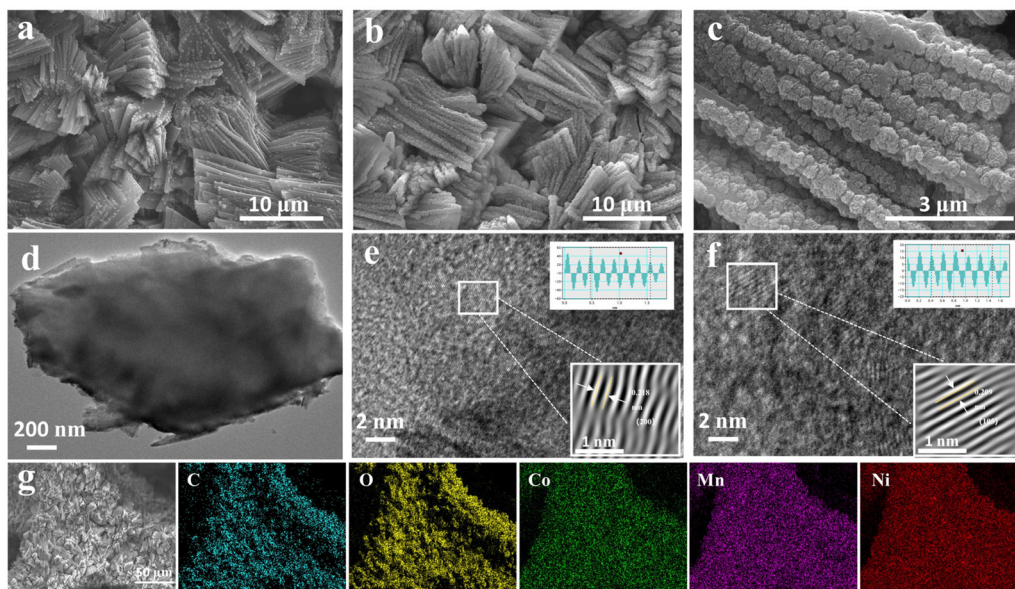


Fig. 3 (a) SEM images of  $\text{Co}_1\text{Ni}_{0.5}\text{Mn}_1\text{BDC@NF}$ . (b and c) SEM images of  $\text{Co}_1\text{Ni}_{0.5}\text{Mn}_1\text{BDC@NF-A}$ . (d) TEM images of  $\text{Co}_1\text{Ni}_{0.5}\text{Mn}_1\text{BDC@NF-A}$ . (e and f) HRTEM images of  $\text{Co}_1\text{Ni}_{0.5}\text{Mn}_1\text{BDC@NF-A}$ . (g) SEM mapping images of  $\text{Co}_1\text{Ni}_{0.5}\text{Mn}_1\text{BDC@NF-A}$ .

flower-shaped small spheres grow less on the curved surface and are not arranged too tightly, resulting in a decrease in the active surface area. In general, the electrocatalytic performance of the synthesized catalysts primarily depends on the number and intrinsic activity of electroactive sites.<sup>43,44</sup> The increase in active area after activation indicates performance enhancement,<sup>45</sup> and the morphological transformation of the catalyst suggests the generation of MOOH. The TEM results show that the catalyst has a thin nanosheet structure with excellent electrocatalytic activity (Fig. 3d). High-resolution TEM images in Fig. 3e and f show the distinct lattice spacings of 0.218 nm and 0.209 nm marked in white, consistent with the (200) planes of CoOOH and the (105) planes of NiOOH, respectively, which matched the XRD results. This indicates that the true active substance of the catalyst after activation is Co/NiOOH. To investigate the role of Mn, we conducted SEM testing on Co<sub>1</sub>Ni<sub>0.5</sub>Mn<sub>1</sub>BDC@NF-A. According to Fig. S7,† it is disorderly stacked on the surface of NF in a sheet-like manner, which covers up some of the active areas compared to the ordered growth of curved sheet-like structures, and no flower-shaped small nanospheres are growing on the sheet-like surface. It can be inferred that the addition of Mn can promote the transformation of morphology, mainly transforming the catalyst from disordered stacking to an ordered staggered arrangement, which exposes more active sites.

The SEM mapping test confirmed the uniform distribution of Co, Ni and Mn metal in the catalyst (Fig. 3g). The EDS results of Co<sub>1</sub>Ni<sub>0.5</sub>Mn<sub>1</sub>BDC@NF and Co<sub>1</sub>Ni<sub>0.5</sub>Mn<sub>1</sub>BDC@NF-A are shown in Fig. S8 and S9,† respectively, with a more significant change in the proportion of C, O and Ni atoms. The increase in Ni content may be due to the influence of Ni in NF, while the change in C and O should be due to the formation of MOOH after activation. TEM mapping and ICP-OES were also employed to determine the elemental content in the samples. Fig. S10† illustrates the uniform distribution of Co, Ni, Mn, C and O. The element ratio is presented in Fig. S11,† where the content of Ni and Mn shows a significant reduction compared to the SEM results. The TEM test results were more accurate than those obtained by SEM (which directly tests on NF) and XPS (which is limited to indicating testing), due to the process of sonicating the catalyst from NF and dissolving it in a dispersant for testing. Additionally, the proportion of metal element content tested by ICP-OES (Table S1†) closely matches that from TEM-EDS. Therefore, the TEM-EDS results should be used as the elemental content reference for the catalyst in this study.

The chemical composition of the surface and the electronic interaction of the samples were revealed using XPS. Fig. S12† presents the XPS survey spectra of Co<sub>1</sub>Ni<sub>0.5</sub>Mn<sub>1</sub>BDC@NF-A and Co<sub>1</sub>Ni<sub>0.5</sub>BDC@NF-A, indicating the coexistence of Ni, Co and Mn. Fig. S13† displays the Ni 2p and Co 2p spectra before and after the activation of Co<sub>1</sub>Ni<sub>0.5</sub>Mn<sub>1</sub>BDC@NF, revealing significant differences in peak shapes and binding energy positions. Compared to the MOF structure, the activated catalyst (Co<sub>1</sub>Ni<sub>0.5</sub>Mn<sub>1</sub>BDC@NF-A) exhibits a lower binding energy of Co/Ni 2p<sub>2/3</sub>, suggesting the formation of Co/NiOOH. Fig. S14†

illustrates the percentage of near-surface elements in Co<sub>1</sub>Ni<sub>0.5</sub>Mn<sub>1</sub>BDC@NF and Co<sub>1</sub>Ni<sub>0.5</sub>BDC@NF obtained through XPS analysis (Table S2†). The addition of manganese partially replaces nickel and cobalt, with a greater inclination towards replacing Co-elements, as evidenced by the intensity of elemental peaks in the entire XPS spectrum. In Fig. S12,† the attenuation of the characteristic peaks of Co is more pronounced compared to that of Ni. More significantly, the metallic atomic ratio on the material surface is determined by examining the proportion of the fitted peaks' areas, indicating an increase in the proportion of Ni<sup>3+</sup> and Co<sup>3+</sup> after the addition of the Mn element (Fig. 4a), which is the reason for the enhanced OER and EOR activity. These results indicate that the addition of Mn can modulate the delocalized electron density around Co and Ni atoms, thereby facilitating the formation of trivalent states of Ni and Co.<sup>46</sup>

High-resolution Co 2p spectra (Fig. 4b) indicate the presence of both trivalent (Co<sup>3+</sup> 2p<sub>3/2</sub> 780.57 eV, Co<sup>3+</sup> 2p<sub>1/2</sub> 795.86 eV) and bivalent (Co<sup>2+</sup> 2p<sub>3/2</sub> 782.50 eV, Co<sup>2+</sup> 2p<sub>1/2</sub> 797.40 eV) forms in Co<sub>1</sub>Ni<sub>0.5</sub>Mn<sub>1</sub>BDC@NF-A.<sup>37</sup> And Ni 2p spectra (Fig. 4c) demonstrate the presence of trivalent (Ni<sup>3+</sup> 2p<sub>3/2</sub> 856.41 eV, Ni<sup>3+</sup> 2p<sub>1/2</sub> 874.25 eV) and bivalent (Ni<sup>2+</sup> 2p<sub>3/2</sub> 855.64 eV, Ni<sup>2+</sup> 2p<sub>1/2</sub> 873.20 eV) forms in Co<sub>1</sub>Ni<sub>0.5</sub>Mn<sub>1</sub>BDC@NF-A.<sup>47</sup> Additionally, in Fig. 4d, the O 1s spectrum of Co<sub>1</sub>Ni<sub>0.5</sub>Mn<sub>1</sub>BDC@NF-A is deconvoluted into three characteristic peaks at 530.28, 531.29 and 531.83 eV, corresponding to ligand skeleton oxygen (C–O), metallic lattice oxygen (M–O) and adsorbed oxygen.<sup>48</sup> By comparing the XPS spectra of Co<sub>1</sub>Ni<sub>0.5</sub>Mn<sub>1</sub>BDC@NF-A and Co<sub>1</sub>Ni<sub>0.5</sub>BDC@NF-A, it is observed that the peak of Co<sup>2+</sup> 2p<sub>3/2</sub> undergoes a positive shift of 0.16 eV after the addition of Mn (Fig. 4b). Similarly, the peak of Ni<sup>2+</sup> 2p<sub>3/2</sub> experiences a positive shift of 0.11 eV (Fig. 4c). Combining XPS fitting peak area analysis, which shows that the catalyst added by Mn exhibits larger Co<sup>3+</sup>/Co<sup>2+</sup> and Ni<sup>3+</sup>/Ni<sup>2+</sup> atomic ratios than Co<sub>1</sub>Ni<sub>0.5</sub>BDC@NF-A, indicates that the incorporation of Mn can regulate the delocalized electron density around Co and Ni atoms. In addition, in Fig. 4d, the peak of M–O experiences a negative displacement of 0.13 eV. This shift can be attributed to the addition of Mn, which exerts a significant electronic regulatory effect on the M–O bond. Previous works have clearly demonstrated, using density functional theory, that catalysts without Mn exhibit a clear band gap in the distribution of the total density of states (TDOS). However, Mn doping causes two split orbitals in the band gap, thereby providing an intermediate energy level for electron transition. The partial density of states (PDOS) indicates that Ni/Co 3d and O 2p orbitals constitute this intermediate level.<sup>49</sup> In this work, the addition of Mn promotes the hybridization of Ni 3d, Co 3d and O 2p orbitals in Co<sub>1</sub>Ni<sub>0.5</sub>Mn<sub>1</sub>BDC@NF-A, lowering the energy barrier for the Co/Ni(II) to Co/Ni(III) transition and thereby facilitating the oxidation of Co<sup>2+</sup>/Ni<sup>2+</sup> into Co<sup>3+</sup>/Ni<sup>3+</sup>, thus enhancing the electrocatalytic kinetics of the OER and EOR.<sup>36,50</sup>

Fig. 4e displays two peaks at 639.44 eV and 652.20 eV, which can be assigned to Mn 2p<sub>3/2</sub> and Mn 2p<sub>1/2</sub> of Mn<sup>2+</sup> species, and two peaks at 642.38 eV and 654.19 eV, corres-

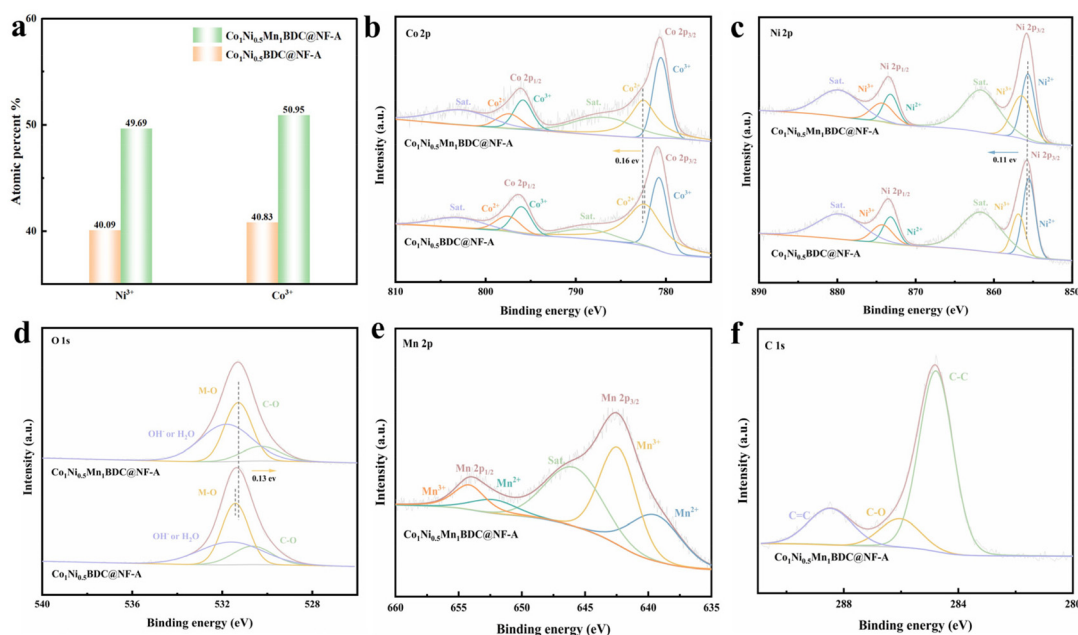


**Fig. 4** (a) The elemental contents of Ni<sup>3+</sup> and Co<sup>3+</sup> in Co<sub>1</sub>Ni<sub>0.5</sub>Mn<sub>1</sub>BDC@NF-A and Co<sub>1</sub>Ni<sub>0.5</sub>BDC@NF-A were determined by XPS peak areas. High-resolution spectra of (b) Co 2p, (c) Ni 2p, and (d) O 1s of Co<sub>1</sub>Ni<sub>0.5</sub>Mn<sub>1</sub>BDC@NF-A and Co<sub>1</sub>Ni<sub>0.5</sub>BDC@NF-A, respectively. (e) High-resolution Mn 2p spectrum of Co<sub>1</sub>Ni<sub>0.5</sub>Mn<sub>1</sub>BDC@NF-A. (f) High-resolution C 1s spectrum of Co<sub>1</sub>Ni<sub>0.5</sub>Mn<sub>1</sub>BDC@NF-A.

ponding to Mn 2p<sub>3/2</sub> and Mn 2p<sub>1/2</sub> of Mn<sup>3+</sup> species, respectively.<sup>48</sup> In Co<sub>1</sub>Ni<sub>0.5</sub>Mn<sub>1</sub>BDC@NF (Fig. S15<sup>†</sup>), Mn exists in both Mn<sup>2+</sup> and Mn<sup>3+</sup> states. After activation, Mn<sup>2+</sup> and Mn<sup>3+</sup> remain present in Co<sub>1</sub>Ni<sub>0.5</sub>Mn<sub>1</sub>BDC@NF-A, but the Mn<sup>2+</sup> peaks in Mn 2p spectra shift towards higher energy levels. This shift is attributed to the oxidation of Mn<sup>2+</sup> under prolonged oxidation potential and its interaction with Co/Ni.<sup>50</sup> These findings suggest the presence of both Mn<sup>2+</sup> and Mn<sup>3+</sup> states in the final sample. Moreover, the peak area fitted by XPS and the shift in Mn<sup>2+</sup> binding energy position indicate a higher content of Mn<sup>3+</sup> compared to Mn<sup>2+</sup>. The changes in electron density around Mn due to activation and the shift in Co/Ni binding energy induced by Mn addition suggest a strong electronic interaction among Co, Mn and Ni. And in Fig. 4f, the C 1s spectrum of Co<sub>1</sub>Ni<sub>0.5</sub>Mn<sub>1</sub>BDC@NF-A is deconvoluted into three characteristic peaks at 284.78, 286.04 and 288.47 eV, corresponding to C-C, C-O, and C=C bonds.<sup>51</sup> Overall, although Mn exhibits poorer activity in oxygen evolution and ethanol oxidation than Co and Ni, it can reduce the energy barrier for Co/Ni(II) to Co/Ni(III) transformation to reduce the reaction voltage of the OER and EOR.<sup>49</sup> Hence, the inclusion of Mn significantly enhances the overall performance of the catalyst.

### 3.2 Electrocatalytic properties for the OER

The OER electrocatalytic performances of all samples were tested in 1 M KOH using a typical three-electrode system at room temperature. Firstly, the prepared catalyst undergoes electrochemical activation by CV, transitioning from a MOF structure to the active substance MOOH for the OER/EOR. A

detailed analysis of the activation process reveals the following: during cycling, the CV curve gradually enlarges, and the current density increases with the number of cycles, peaking before the 50th cycle and then stabilizing, indicating the transformation of the catalyst into a more active material. It is well-known that Co<sup>2+</sup>/Ni<sup>2+</sup> can be oxidized into high-valence species.<sup>52</sup> Therefore, the increase in the oxidation peak area in Fig. S2<sup>†</sup> can be attributed to the redox reaction between Co<sup>2+</sup>/Ni<sup>2+</sup> and Co<sup>3+</sup>/Ni<sup>3+</sup>. Based on this analysis, it can be inferred that CoNiBDC, composed of carboxylic acid ligands, undergoes facile hydrolysis on the surface in alkaline electrolyte, rapidly producing Co/Ni(OH)<sub>2</sub> (CoNiBDC + 2OH<sup>-</sup> → Co/Ni(OH)<sub>2</sub> + BDC<sup>2-</sup>),<sup>53</sup> which subsequently further oxidizes to Co/NiOOH (Co<sup>2+</sup>/Ni<sup>2+</sup> ↔ Co<sup>3+</sup>/Ni<sup>3+</sup> + e<sup>-</sup>).<sup>54</sup> The use of BDC as a ligand facilitates the coordination of Ni and Co in the catalyst with six oxygen species, enabling rapid dissociation into hydroxides in alkaline solutions and accelerating the reaction.<sup>52</sup> As depicted in Fig. 5a, the CV curve confirmed the excellent OER activities of Co<sub>1</sub>Ni<sub>0.5</sub>Mn<sub>1</sub>BDC@NF-A at different current densities. To explore the role of the Mn element, electrochemical experiments were conducted on bimetallic systems containing Co<sub>1</sub>Mn<sub>1</sub>BDC@NF-A, Ni<sub>1</sub>Mn<sub>1</sub>BDC@NF-A and Co<sub>1</sub>Ni<sub>0.5</sub>BDC@NF-A. For Co<sub>1</sub>Mn<sub>1</sub>BDC@NF-A and Ni<sub>1</sub>Mn<sub>1</sub>BDC@NF-A, manganese enhances the OER electrochemical performance by promoting the generation of high-valence nickel or cobalt (Fig. S16 and S17<sup>†</sup>). However, unlike bimetallic systems, there exists a synergistic effect between nickel and cobalt in the three-metal systems (Fig. S18<sup>†</sup>).<sup>55</sup> Then, the addition of Mn replaces the positions of Co and Ni, disrupting the synergistic effect, while the OER activity of Mn

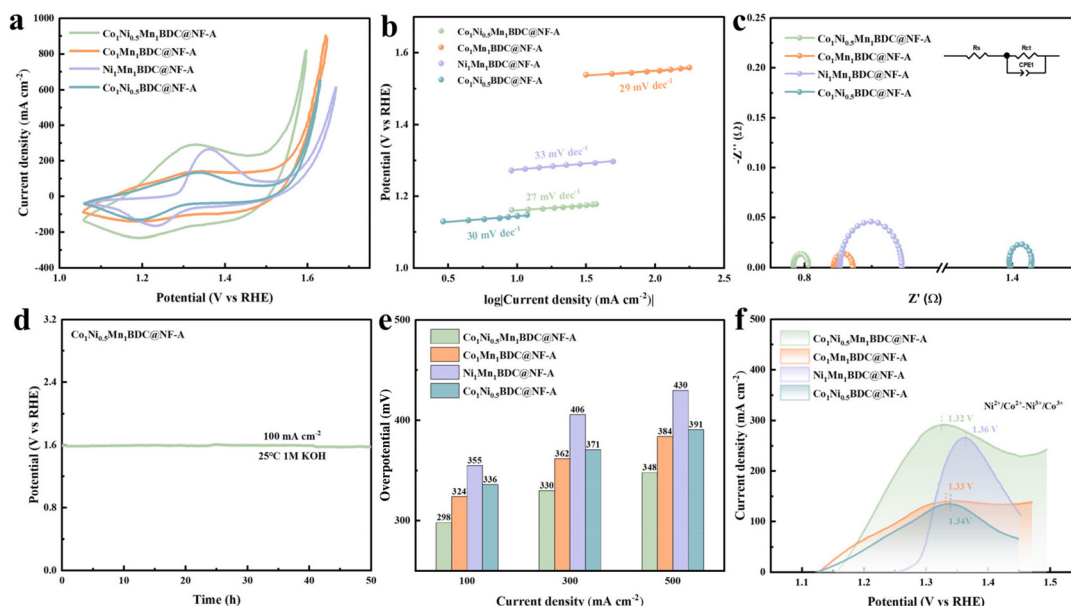


**Fig. 5** Electrochemical OER in 1 M KOH. (a) The cyclic voltammograms of different catalysts. (b) Tafel plots obtained from (a). (c) EIS Nyquist plots. (d) Long-term stability curve for achieving  $100 \text{ mA cm}^{-2}$  with  $\text{Co}_1\text{Ni}_{0.5}\text{Mn}_1\text{BDC@NF-A}$ . (e) Overpotentials needed at current densities of 100, 300 and  $500 \text{ mA cm}^{-2}$  for different samples. (f) Comparison of oxidation peaks on partial CV curves.

is inferior to that of Co and Ni. Therefore, considering the above two aspects, the addition of Mn should theoretically reduce OER performance. However, as shown in Fig. 5a, the voltage of  $\text{Co}_1\text{Ni}_{0.5}\text{Mn}_1\text{BDC@NF-A}$  is significantly lower than that of  $\text{Co}_1\text{Ni}_{0.5}\text{Mn}_1\text{BDC@NF-A}$  at different current densities, which underscores the role of Mn in promoting the generation of high-valent nickel and cobalt to enhance the electrochemical performance of the OER. By analyzing the CV plot, it was observed that  $\text{Co}_1\text{Ni}_{0.5}\text{Mn}_1\text{BDC@NF-A}$  exhibits an overpotential of 298 mV at  $100 \text{ mA cm}^{-2}$  and 348 mV at  $500 \text{ mA cm}^{-2}$ , which surpass those of  $\text{Co}_1\text{Mn}_1\text{BDC@NF-A}$ ,  $\text{Ni}_1\text{Mn}_1\text{BDC@NF-A}$ ,  $\text{Co}_1\text{Ni}_{0.5}\text{BDC@NF-A}$  (Fig. 5e) and other reported nickel-based and cobalt-based catalysts (Table S3†).

Furthermore,  $\text{Co}_1\text{Ni}_{0.5}\text{Mn}_1\text{BDC@NF-A}$  demonstrates the quickest catalytic reaction kinetics, as evidenced by its lowest Tafel slope of  $27 \text{ mV dec}^{-1}$  (Fig. 5b). As illustrated in Fig. 5c, the beneficial electronic structure modification due to Mn addition leads to  $\text{Co}_1\text{Ni}_{0.5}\text{Mn}_1\text{BDC@NF-A}$  having the lowest interfacial charge transfer resistance ( $R_{\text{ct}} = 0.021 \Omega$ ) (Table S4†), a crucial factor in enhancing the OER. Mn can also reduce the solution impedance ( $R_s$ ), which can also be observed in bimetallic systems (Fig. S16c, f and S17c, f†). The stability of electrocatalysts is also a crucial aspect to consider, especially in practical industrial applications. Chronopotentiometry is employed to measure the stability of the optimal sample. The catalyst maintains stability for 50 hours at  $100 \text{ mA cm}^{-2}$  (Fig. 5d). To further demonstrate its stability, the composition, morphology and electronic structure of the samples after stability testing were examined using XRD, SEM and XPS, respectively. The XRD analysis still reveals a peak corresponding to an amorphous thin-layered structure,

indicating that the material composition of the catalyst has not changed and that the catalyst still consists of MOOH (Fig. S19†). As shown in Fig. S20b,† after stability testing, it retains its curved and orderly arrangement into a layered structure. The basic morphology of the catalyst remains mostly unaltered, confirming its stability. However, when working for a long time within the oxidation voltage range, the structure undergoes slight changes due to surface reconstruction and the generation of hydroxides, with most of the nanoflower-shaped balls on the flake disappearing (Fig. S20d†). In fact, the disappearance of small balls also has traces to follow. Before conducting stability testing on  $\text{Co}_1\text{Ni}_{0.5}\text{Mn}_1\text{BDC@NF-A}$ , some small balls (Fig. S20c†) have already adhered to the surface. XPS analysis shows that after long-term stability testing, there is no significant shift in the electronic energy level, which further proves the profound stability (Fig. S21†). The excellent stability of the catalysts can be attributed to several factors: (1) utilizing an MOF as a precursor provides spatial confinement for BDC ligands, ensuring the complete dispersion and stability of active cobalt and nickel sites. (2)  $\text{Co}_1\text{Ni}_{0.5}\text{Mn}_1\text{BDC@NF-A}$  synthesized through MOF reconstruction has a stable nanosheet like structure. (3) Before and after activation, the changes in electron density around Mn, Co and Ni indicate a strong electronic interaction between Co, Mn and Ni. (4) The hybridization effect between Co/Ni 3d and O 2p, enhanced by Mn addition, strengthens the electronic interaction between the metal and oxygen, thereby promoting catalyst stability. The above analysis proves that the sample can improve activity while still ensuring excellent stability.

Furthermore, as illustrated in Fig. 5f, the size of the oxidation peak corresponds to the oxidation process of Co and Ni

(from  $\text{Co}^{2+}/\text{Ni}^{2+}$  to  $\text{Co}^{3+}/\text{Ni}^{3+}$ ), where a larger oxidation peak indicates a higher content of  $\text{Co}^{3+}$  and  $\text{Ni}^{3+}$ . The notable disparity in oxidation peak size between  $\text{Co}_1\text{Ni}_{0.5}\text{Mn}_1\text{BDC@NF-A}$  and  $\text{Co}_1\text{Ni}_{0.5}\text{BDC@NF-A}$  underscores the role of Mn in promoting the formation of high-valence Ni and Co states. This observation aligns with the electronic level analysis of XPS mentioned above, suggesting that the addition of Mn can lower this energy barrier by promoting the hybridization of Co/Ni 3d with O 2p orbitals, resulting in the generation of numerous Co/Ni(III) ions at low bias. The role of Mn addition in promoting the formation of high-valence metals has been demonstrated through both structural and electrochemical properties.

### 3.3 Electrocatalytic properties for the EOR

The EOR electrocatalytic performance of the catalysts was assessed using a typical three-electrode system, which had the same electrode configuration as that used to measure the OER activity, except that the electrolytic solution was replaced with 1 M ethanol in 1 M KOH. The LSV polarization curves presented in Fig. 6a at  $2 \text{ mV s}^{-1}$  were utilized to compare the catalytic performances of the various catalysts in the EOR. As anticipated,  $\text{Co}_1\text{Ni}_{0.5}\text{Mn}_1\text{BDC@NF-A}$  exhibits a lower voltage of approximately 1.30 V vs. RHE ( $@100 \text{ mA cm}^{-2}$ ) compared to  $\text{Ni}_1\text{Mn}_1\text{BDC@NF-A}$  (1.31 V),  $\text{Co}_1\text{Mn}_1\text{BDC@NF-A}$  (1.32 V) and  $\text{Co}_1\text{Ni}_{0.5}\text{BDC@NF-A}$  (1.33 V). This potential is also notably low compared with those of previously reported new nickel-based and cobalt-based EOR catalysts (Table S5<sup>†</sup>). In the electrochemical testing of the EOR, the comparison between  $\text{Co}_1\text{Ni}_{0.5}\text{Mn}_1\text{BDC@NF-A}$  and  $\text{Co}_1\text{Ni}_{0.5}\text{BDC@NF-A}$  at different current densities is more significant. The reason for this is that the improvement in EOR performance is mainly attrib-

ted to the generation of high-valence Ni and Co. Because the mechanism of the EOR on the Ni surface is as follows<sup>56</sup> (the reaction on the Co surface is the same as that on the Ni surface): (1)  $\text{Ni}(\text{OH})_2 + \text{OH}^- \rightarrow \text{NiOOH} + \text{H}_2\text{O} + \text{e}^-$ ; (2)  $\text{NiOOH} + \text{C}_2\text{H}_5\text{OH} \rightarrow \text{CH}_3\text{CHO} + \text{Ni}(\text{OH})_2$ , the EOR reaction requires the generation of  $\text{Ni}^{3+}/\text{Co}^{3+}$ , and a higher content of  $\text{Ni}^{3+}/\text{Co}^{3+}$  corresponds to a faster reaction rate. The focus is on the process and results of the generation of  $\text{Ni}^{3+}$  and  $\text{Co}^{3+}$ , while the partial substitution of Co and Ni with Mn has a relatively minor impact. Therefore, whether it is a bimetallic system (Fig. S22 and S23<sup>†</sup>) or a triple metal system, Mn has a significant effect on enhancing ethanol oxidation reaction performance. The Tafel slope of  $\text{Co}_1\text{Ni}_{0.5}\text{Mn}_1\text{BDC@NF-A}$  is  $31 \text{ mV dec}^{-1}$ , lower than those of  $\text{Ni}_1\text{Mn}_1\text{BDC@NF-A}$  ( $35 \text{ mV dec}^{-1}$ ),  $\text{Co}_1\text{Mn}_1\text{BDC@NF-A}$  ( $46 \text{ mV dec}^{-1}$ ) and  $\text{Co}_1\text{Ni}_{0.5}\text{BDC@NF-A}$  ( $57 \text{ mV dec}^{-1}$ ) (Fig. 6b), indicating that it has the fastest catalytic reaction kinetics in the EOR. In Fig. 6c, the  $R_{\text{ct}}$  in  $\text{Co}_1\text{Ni}_{0.5}\text{Mn}_1\text{BDC@NF-A}$  is  $0.015 \Omega$  (Table S6<sup>†</sup>) due to the positive optimization of the electronic structure caused by Mn addition. Consistent with the OER, it can reduce the solution impedance ( $R_s$ ) /  $\Omega$ , which can also be reflected in the bi-metallic system (Fig. S22c and S23c<sup>†</sup>). Stability was evaluated through chronopotentiometry, which shows that it was maintained for 50 hours at  $100 \text{ mA cm}^{-2}$  (Fig. 6d). Similarly, we conducted XRD, SEM, and XPS tests on the samples after EOR stability testing (Fig. S24–S26<sup>†</sup>). The results are similar to those of the OER, that is, the main active components are still CoOOH and NiOOH, and the layered structure and the electronic structure have not changed significantly. The above results once again prove the excellent stability of  $\text{Co}_1\text{Ni}_{0.5}\text{Mn}_1\text{BDC-A}$ .

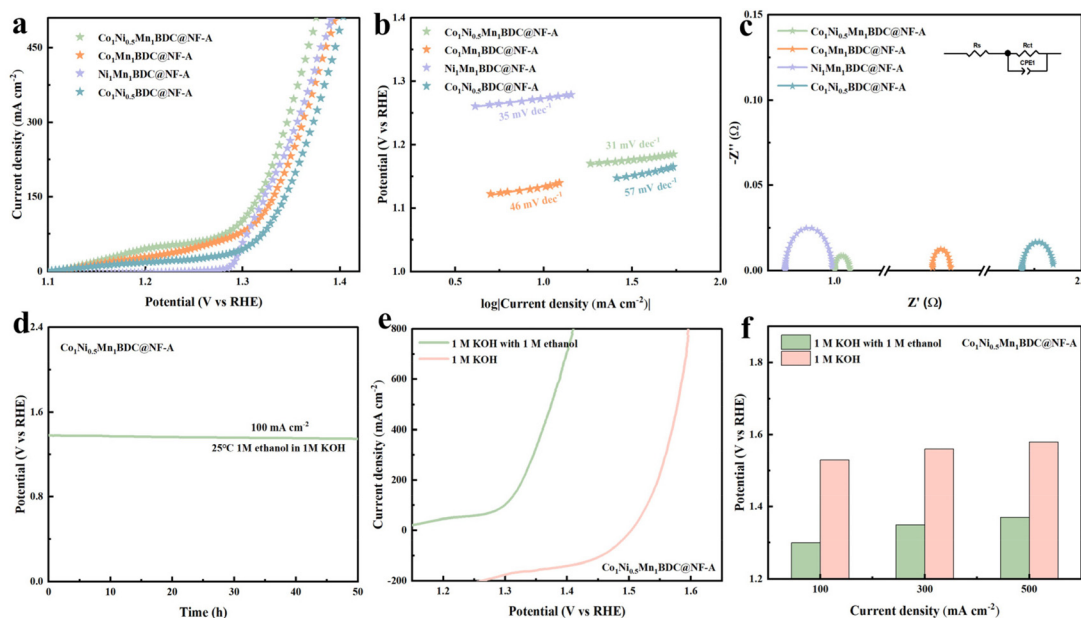


**Fig. 6** Electrocatalytic EOR in 1 M KOH with 1 M ethanol. (a) The polarization curves of different catalysts at  $2 \text{ mV s}^{-1}$ . (b) Tafel plots obtained from (a). (c) EIS Nyquist plots. (d) Long-term stability curve to drive  $100 \text{ mA cm}^{-2}$  of  $\text{Co}_1\text{Ni}_{0.5}\text{Mn}_1\text{BDC@NF-A}$ . Comparison of the EOR and OER in (e) the polarization curves (f) and the potentials required at current densities of 100, 300 and  $500 \text{ mA cm}^{-2}$ .



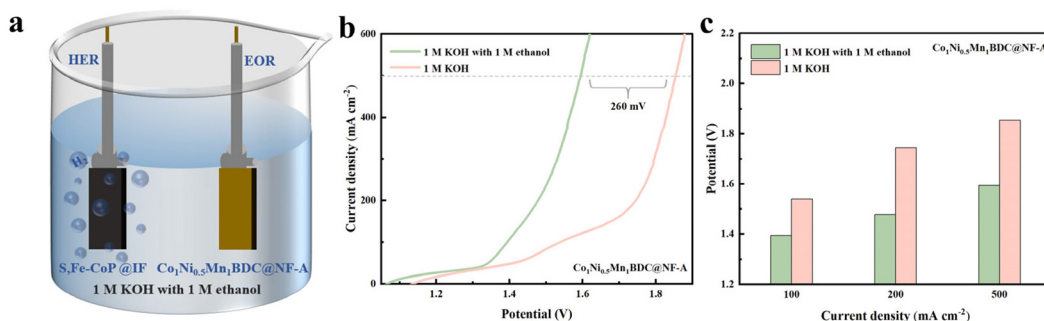


**Fig. 7** (a) Schematic diagram of a two-electrode system. (b) Comparison of the polarization curves for  $\text{Co}_1\text{Ni}_{0.5}\text{Mn}_1\text{BDC@NF-A}$  during water splitting in 1 M KOH with and without 1 M ethanol and (c) the potentials at different current densities.

Adjusting the proportion of the three metals has always been a challenge in determining the optimal performance of the catalyst. We conducted multiple comparative experiments to adjust the optimal proportions of the three metals (Fig. S27a and c†). Due to the best OER performance of the bimetallic catalyst  $\text{Co}_1\text{Mn}_1\text{BDC@NF-A}$ , it was decided to use this as a basis to search for the best-performing bifunctional catalyst by changing the Ni element content (Fig. S27b and d†). Furthermore, as shown in Fig. 6e and f, there is a notable voltage disparity between the OER and EOR. The ethanol oxidation reaction requires only 1.30 V to achieve  $100 \text{ mA cm}^{-2}$  and 1.37 V to reach  $500 \text{ mA cm}^{-2}$ , significantly lower than the oxygen evolution reaction, which requires 1.53 V to achieve  $100 \text{ mA cm}^{-2}$  and 1.58 V to reach  $500 \text{ mA cm}^{-2}$ . To further reduce the energy requirement for hydrogen production, one solution is to substitute the OER with the EOR.

### 3.4 Overall water electrolysis efficiency

Inspired by the outstanding electrocatalytic performance and long-term stability exhibited by  $\text{Co}_1\text{Ni}_{0.5}\text{Mn}_1\text{BDC@NF-A}$  in both the OER and EOR, it was employed as the anode in a two-electrode system to assess water-splitting voltage. The cathode of the two-electrode system is S, Fe-CoP, synthesized in the laboratory (Fig. S28†). The overall water decomposition diagram is illustrated in Fig. 7a. In Fig. 7b, the LSV curves of  $\text{Co}_1\text{Ni}_{0.5}\text{Mn}_1\text{BDC@NF-A}$  during water splitting in 1 M KOH with and without 1 M ethanol for OER and EOR have been demonstrated. To attain a current density of  $100 \text{ mA cm}^{-2}$ , the ethanol-water mixture requires just 1.39 V, markedly less than the voltage needed for the system lacking ethanol, which is 1.54 V. Similarly, comparable results are observed at higher currents. At  $500 \text{ mA cm}^{-2}$ , the OER-HER system requires 1.85 V, considerably higher than the EOR-HER system (1.59 V) (Fig. 7c). This demonstrates that utilizing the EOR as the anode for hydrogen production *via* water electrolysis is one method to enhance hydrogen production efficiency.

In summary, the robust catalytic activity of  $\text{Co}_1\text{Ni}_{0.5}\text{Mn}_1\text{BDC@NF-A}$  can be attributed to the following reasons: (1) the high conductivity of Ni foam facilitates mass and electron transfer. (2) Benzene-1,4-dicarboxylic acid (PTA) with a *para*-conjugated benzene ring exhibits excellent electron

delocalization and conductivity. (3) The uniform incorporation of Mn enables the *in situ* generation of MOFs with a well-organized layered nanosheet morphology,<sup>57</sup> facilitating the accessibility of catalytic sites for the OER and EOR. (4) The addition of Mn promotes the hybridization effect between Ni, Co and O, facilitating the generation of Co/Ni(III) species, thereby accelerating the reaction kinetics of both the OER and EOR.

## 4. Conclusion

In summary,  $\text{Co}_1\text{Ni}_{0.5}\text{Mn}_1\text{BDC@NF}$ , synthesized through a simple one-step hydrothermal method, was transformed into the actual active substances CoOOH and NiOOH after CV activation, exhibiting excellent electrochemical performance in both the OER (with an overpotential of 298 mV at  $100 \text{ mA cm}^{-2}$ ) and EOR (with a potential of 1.30 V at  $100 \text{ mA cm}^{-2}$ ). Moreover, it showed stable operation in the EOR and OER during a 50-hour stability test. The addition of Mn not only adjusted the hybridization effect between Ni, Co and O, promoting the conversion of  $\text{Ni}^{2+}$  to  $\text{Ni}^{3+}$  and  $\text{Co}^{2+}$  to  $\text{Co}^{3+}$ , but also assisted in structural transformation, thereby enhancing the efficiency of the OER and EOR. Additionally, the combination of the EOR and HER only needs 1.39 V and that of OER and HER only requires 1.54 V to reach  $100 \text{ mA cm}^{-2}$ , which is much lower than those of the other two electrode hydrogen production systems. The successful synthesis of  $\text{Co}_1\text{Ni}_{0.5}\text{Mn}_1\text{BDC@NF-A}$ , a non-precious metal catalyst, provides insights into achieving efficient and stable hydrogen production.

## Conflicts of interest

There are no conflicts to declare.

## Acknowledgements

This work was supported by grants from the Key R&D Program of Shandong Province, China (2021ZLGX06), and the National

Natural Science Foundation of China (Grant No. 52274308, 52174283 and U22B20144).

## References

- 1 L. Zhang, Z. Yan, X. Chen, M. Yu, F. Liu, F. Cheng and J. Chen, Facile synthesis of amorphous MoS<sub>x</sub>-Fe anchored on Zr-MOFs towards efficient and stable electrocatalytic hydrogen evolution, *Chem. Commun.*, 2020, **56**, 2763–2766.
- 2 J. Li, F. Liu, M. Yu, H. Hu, H. Liu and F. Cheng, Interfacial Engineering of Ni-Fe Based Electrocatalysts for Robust Oxygen Evolution, *J. Phys. Chem. C*, 2021, **125**(46), 25383–25391.
- 3 Y. Tang, Q. Liu, L. Dong, H. B. Wu and X. Y. Yu, Activating the hydrogen evolution and overall water splitting performance of NiFe LDH by cation doping and plasma reduction, *Appl. Catal., B*, 2020, **266**, 118627.
- 4 P. Yan, Q. Liu, H. Zhang, L. Qiu, H. B. Wu and X. Y. Yu, Deeply reconstructed hierarchical and defective NiOOH/FeOOH nanoboxes with accelerated kinetics for the oxygen evolution reaction, *J. Mater. Chem. A*, 2021, **9**, 15586–15594.
- 5 Y. Chen, P. Liao, K. Jin, Y. Zheng, H. Shao and G. Li, Current progress in metal-organic frameworks and their derivatives for electrocatalytic water splitting, *Inorg. Chem. Front.*, 2023, **10**, 6489–6505.
- 6 L. Deng, S. Hung, S. Zhao, W. Zeng, Z. Lin, F. Hu, Y. Xie, L. Yin, L. Li and S. Peng, Unveiling coordination transformation for dynamically enhanced hydrogen evolution catalyst, *Energy Environ. Sci.*, 2023, **16**, 5220.
- 7 W. Zhang, Y. Tang, L. Yu and X. Yu, Activating the alkaline hydrogen evolution performance of Mo-incorporated Ni(OH)<sub>2</sub> by plasma-induced heterostructure, *Appl. Catal., B*, 2020, **260**, 118154.
- 8 L. Zhang, J. Wang, K. Jiang, Z. Xiao, Y. Gao, S. Lin and B. Chen, Self-Reconstructed Metal-Organic Framework Heterojunction for Switchable Oxygen Evolution Reaction, *Angew. Chem., Int. Ed.*, 2022, **61**, e202214794.
- 9 Z. Xue, K. Liu, Q. Liu, Y. Li, M. Li, C. Su, N. Ogiwara, H. Kobayashi, H. Kitagawa, M. Liu and G. Li, Missing-Linker Metal-Organic Frameworks for Oxygen Evolution Reaction, *Nat. Commun.*, 2019, **10**, 5048.
- 10 N. Zhang, Y. Hu, L. An, O. Li, J. Yin, J. Li, R. Yang, M. Lu, S. Zhang, P. Xi and C. Yan, Surface Activation and Ni-S Stabilization in NiO/NiS<sub>2</sub> for Efficient Oxygen Evolution Reaction, *Angew. Chem., Int. Ed.*, 2022, **61**, e202207217.
- 11 A. Loncar, D. Lpez, S. Cherevko and N. Hodnik, Interrelationships between Oxygen Evolution and Iridium Dissolution Mechanisms, *Angew. Chem., Int. Ed.*, 2022, **61**, e202114437.
- 12 K. Svane and J. Rossmeisl, Theoretical Optimization of Compositions of High-Entropy Oxides for the Oxygen Evolution Reaction, *Angew. Chem., Int. Ed.*, 2022, **61**, e202201146.
- 13 F. Ren, Z. Zhang, Z. Liang, Q. Shen, Y. Luan, R. Xing, Z. Fei and Y. Du, Synthesis of PtRu alloy nanofireworks as effective catalysts toward glycerol electro-oxidation in alkaline media, *J. Colloid Interface Sci.*, 2022, **608**, 800–808.
- 14 T. Wang, X. Cao and L. Jiao, Progress in Hydrogen Production Coupled with Electrochemical Oxidation of Small Molecules, *Angew. Chem., Int. Ed.*, 2022, **61**, e202213328.
- 15 T. Wang, L. Miao, S. Zheng, H. Qin, X. Cao, L. Yang and L. Jiao, Interfacial Engineering of NiN/MoN Heterojunctions for Urea Assisted Hydrogen Evolution Reaction, *ACS Catal.*, 2023, **13**, 4091–4100.
- 16 H. Wang, A. Guan, J. Zhang, Y. Mi, S. Li, T. Yuan, C. Jing, L. Zhang, L. Zhang and G. Zheng, Copper-doped nickel oxyhydroxide for efficient electrocatalytic ethanol oxidation, *Chin. J. Catal.*, 2022, **43**, 1478–1484.
- 17 S. Ren, D. Du, L. Ma and C. Li, Mesoporous PdBi film as efficient electrocatalyst for ethanol oxidation reaction, *J. Phys.: Mater.*, 2021, **4**, 034001.
- 18 H. Sun, L. Li, Y. Chen, H. Kim, X. Xu, D. Guan, Z. Hu, L. Zhang, Z. Shao and W. Jung, Boosting ethanol oxidation by NiOOH-CuO nano-heterostructure for energy-saving hydrogen production and biomass upgrading, *Appl. Catal., B*, 2023, **325**, 122388.
- 19 H. Xiao, S. Xue, J. Zhang, M. Zhao, J. Ma, S. Chen, Z. Zheng, J. Jia and H. Wu, Facile electrolytic synthesis of Pt and carbon quantum dots coloaded multiwall carbon nanotube as highly efficient electrocatalyst for hydrogen evolution and ethanol oxidation, *Chem. Eng. J.*, 2021, **408**, 127271.
- 20 Y. Chen, J. Seo, Y. Sun, T. Wynn, M. Olguin, M. Zhang, J. Wang, S. Xi, Y. Du, K. Yuan, W. Chen, A. Fisher, M. Wang, Z. Feng, J. Gracia, L. Huang, S. Du, H. Gao, Y. Meng and Z. Xu, Enhanced oxygen evolution over dual corner-shared cobalt tetrahedra, *Nat. Commun.*, 2022, **13**, 5510.
- 21 Y. Hao, S. Hung, W. Zeng, Y. Wang, C. Zhang, C. Kuo, L. Wang, S. Zhao, Y. Zhang, H. Chen and S. Peng, Switching the Oxygen Evolution Mechanism on Atomically Dispersed Ru for Enhanced Acidic Reaction Kinetics, *J. Am. Chem. Soc.*, 2023, **145**, 23659–23669.
- 22 S. Zhao, Y. Wang, Y. Hao, L. Yin, C. Kuo, H. Chen, L. Li and S. Peng, Lewis Acid Driving Asymmetric Interfacial Electron Distribution to Stabilize Active Species for Efficient Neutral Water Oxidation, *Adv. Mater.*, 2024, **36**, 2308925.
- 23 C. Xiang, D. Zeng, B. Du, X. Huang, H. Lin, P. Zhang, Z. Zhang, D. Chen, W. Li and Y. Meng, Regulation of the electronic structure and surface wettability of a Co<sub>9</sub>S<sub>8</sub> electrocatalyst by nitrogen and phosphorous Co-doping for efficient overall water splitting, *Inorg. Chem. Front.*, 2023, **10**, 6964–6975.
- 24 D. Shi, Y. Ji, F. Lu, J. Yao, S. Zhang and P. Zhang, Oxygen vacancies meet partial S substitution: an effective strategy to achieve obvious synergistic effects and adjustable electrochemical behavior in NiFe-LDH for enhanced OER and capacitive performance, *Inorg. Chem. Front.*, 2023, **10**, 5391–5405.
- 25 Z. Zhang, Y. Dong, C. Carlos and X. Wang, Surface Ligand Modification on Ultrathin Ni(OH)<sub>2</sub>, Nanosheets Enabling

- Enhanced Alkaline Ethanol Oxidation Kinetics, *ACS Nano*, 2023, **17**, 17180–17189.
- 26 S. Zhao, F. Hu, L. Yin, L. Li and S. Peng, Manipulating electron redistribution induced by asymmetric coordination for electrocatalytic water oxidation at a high current density, *Sci. Bull.*, 2023, **68**, 1389–1398.
- 27 S. Wang, Q. Li, S. Sun, K. Ge, Y. Zhao, K. Yang, Z. Zhang, J. Cao, J. Lu, Y. Yang, Y. Zhang, M. Pan, Z. Lin and L. Zhu, Heterostructured ferroelectric BaTiO<sub>3</sub>@MOF-Fe/Co electrocatalysts for efficient oxygen evolution reaction, *J. Mater. Chem. A*, 2022, **10**, 5350.
- 28 Y. Shi, J. Cai, X. Zhang, Z. Li and S. Lin, Promotional effects of trace Ni on its dualfunctional electrocatalysis of Co/N-doped carbon, international journal of hydrogen energy, *Int. J. Hydrogen Energy*, 2022, **47**, 7761–7769.
- 29 Y. Li, Y. Xu, C. Li, W. Zhu, W. Chen, Y. Zhao, R. Liu and L. Wang, ZIF-67-Derived NiCo-Layered Double Hydroxide@Carbon Nanotube Architectures with Hollow Nanocage Structures as Enhanced Electrocatalysts for Ethanol Oxidation Reaction, *Molecules*, 2023, **28**, 1173.
- 30 Y. Cao, T. Wang, X. Li, L. Zhang, Y. Luo, F. Zhang, A. M. Asiri, J. Hu, Q. Liu and X. Sun, A hierarchical CuO@NiCo layered double hydroxide core-shell nanoarray as an efficient electrocatalyst for the oxygen evolution reaction, *Inorg. Chem. Front.*, 2021, **8**, 3049–3054.
- 31 S. Yagi, I. Yamada, H. Tsukasaki, A. Seno, M. Murakami, H. Fujii, H. Chen, N. Umezawa, H. Abe, N. Nishiyama and S. Mori, Covalency-reinforced oxygen evolution reaction catalyst, *Nat. Commun.*, 2015, **6**, 8249.
- 32 S. Hirai, S. Yagi, W. T. Chen, F. C. Chou, N. Okazaki, T. Ohno, H. Suzuki and T. Matsuda, Non-Fermi Liquids as Highly Active Oxygen Evolution Reaction Catalysts, *Adv. Sci.*, 2017, **4**, 1700176.
- 33 Y. Zhou, F. Li, B. Dong and Y. Chai, Double self-reinforced coordination modulation constructing stable Ni<sup>4+</sup> for water oxidation, *Energy Environ. Sci.*, 2024, **17**, 1468.
- 34 N. Selvam, S. Kwak, G. Choi, M. Oh, H. Kim, W. Yoon, W. Lee and P. Yoo, Unveiling the Impact of Fe Incorporation on Intrinsic Performance of Reconstructed Water Oxidation Electrocatalyst, *ACS Energy Lett.*, 2021, **6**, 4345–4354.
- 35 M. Han, N. Wang, B. Zhang, Y. J. Xia, J. Li, J. R. Han, K. L. Yao, C. C. Gao, C. N. He, Y. C. Liu, Z. M. Wang, A. Seifitokaldani, X. H. Sun and H. Y. Liang, High-Valent Nickel Promoted by Atomically Embedded Copper for Efficient Water Oxidation, *ACS Catal.*, 2020, **10**, 9725–9734.
- 36 Y. Gan, M. Cui, X. Dai, Y. Ye, F. Nie, Z. Ren, X. Yin, B. Wu, Y. Cao, R. Cai and X. Zhang, Mn-doping induced electronic modulation and rich oxygen vacancies on vertically grown NiFe<sub>2</sub>O nanosheet array for synergistically triggering oxygen evolution reaction, *Nano. Res.*, 2022, **15**, 3940–3945.
- 37 R. Fan, H. Zhao, Y. Zhen, F. Wang, H. Hu, Y.-M. Chai and B. Dong, Mn-induced strengthening hybridization effect of Co–O bond for stable oxygen evolution in acidic media, *Fuel*, 2023, **333**, 126361.
- 38 L. Zhou, D. Feng, C. Liu, Y. Sun, Y. Fu and T. Ma, Amorphous Ni(OH)<sub>2</sub>-Ni<sub>3</sub>S<sub>2</sub>/NF nano-flower heterostructure catalyst promotes efficient urea assisted overall water splitting, *Chem. – Asian J.*, 2024, e202300980.
- 39 N. Xu, F. Wang, J. Han, W. Yu, W. Li, Y. Li, Y. Zhou, Y. Chai and B. Dong, Fe, S-uniformly dispersed Ni MOFs based on FeS substrate precipitation-dissolution equilibrium for water and seawater oxidation, *Inorg. Chem. Front.*, 2023, **10**, 7193.
- 40 N. Karthikeyan, J. Prince, S. Ramalingam and S. Periandy, Electronic [UV-Visible] and vibrational [FT-IR, FT-Raman] investigation and NMR-mass spectroscopic analysis of terephthalic acid using quantum Gaussian calculations, *Spectrochim. Acta, Part A*, 2015, **139**, 229–242.
- 41 Z. Zou, T. Wang, X. Zhao, W. Jiang, H. Pan, D. Gao and C. Xu, Expediting *in situ* Electrochemical Activation of Two-Dimensional Metal-Organic Frameworks for Enhanced OER Intrinsic Activity by Iron Incorporation, *ACS Catal.*, 2019, **9**(8), 7356–7364.
- 42 L. Wang, L. Song, Z. Yang, Y. Chang, F. Hu, L. Li, L. Li, H. Chen and S. Peng, Electronic Modulation of Metal-Organic Frameworks by Interfacial Bridging for Efficient pH-Universal Hydrogen Evolution, *Adv. Funct. Mater.*, 2023, **33**, 2210322.
- 43 B. Qin, X. Zhao, Q. Wang, W. Yao, Y. Cai, Y. Chen, P. Wang, Y. Zou, J. Cao, X. Zheng, J. Qi and W. Cai, A tandem electrocatalyst with dense heterointerfaces enabling the stepwise conversion of polysulfide in lithium-sulfur batteries, *Energy Storage Mater.*, 2023, **55**, 445–454.
- 44 Y. Yan, J. Lin, J. Cao, S. Guo, X. Zheng, D. Feng and J. Qi, Activating and optimizing the activity of NiCoP nanosheets for electrocatalytic alkaline water splitting through the V doping effect enhanced by P vacancies, *J. Mater. Chem. A*, 2019, **7**, 24486.
- 45 Y. Yan, J. Lin, K. Huang, X. Zheng, L. Qiao, S. Liu, J. Cao, S. Jun, Y. Yamauchi and J. Qi, Tensile Strain-Mediated Spinel Ferrites Enable Superior Oxygen Evolution Activity, *J. Am. Chem. Soc.*, 2023, **145**, 24218–24229.
- 46 Y. Huang, X. Zhao, F. Tang, X. Zheng, W. Cheng and W. Che, Strongly electrophilic heteroatoms confined in atomic CoOOH nanosheets realizing efficient electrocatalytic water oxidation, *J. Mater. Chem. A*, 2018, **6**, 3202.
- 47 Z. Li, S. Ning, J. Xu, J. Zhu, Z. Yuan, Y. Wu, J. Chen, F. Xie, Y. Jin, N. Wang, H. Meng and S. Sun, In situ electrochemical activation of Co(OH)<sub>2</sub>@Ni(OH)<sub>2</sub> heterostructures for efficient ethanol electrooxidation reforming and innovative zinc-ethanol-air batteries, *Energy Environ. Sci.*, 2022, **15**, 5300.
- 48 S. Chen, H. Liao, X. Xu, R. Wang, Z. Sun and L. Huang, Ga-induced electronic structure engineering of NiFe<sub>2</sub>O<sub>4</sub> nanosheet arrays for stable and efficient oxygen evolution, *Inorg. Chem. Front.*, 2023, **10**, 6320.
- 49 Y. Zhang, C. Cheng, C. Kuai, D. Sokaras, X. Zheng, S. Sainio, F. Lin, C. Dong, D. Nordlund and X. Du, Unveiling the critical role of the Mn dopant in a NiFe(OH)<sub>2</sub> catalyst for water oxidation, *J. Mater. Chem. A*, 2020, **8**, 17471.
- 50 Y. Liu, N. Ran, R. Ged, J. Liu, W. Li, Y. Chen, L. Feng and R. Che, Porous Mn-doped cobalt phosphide nanosheets as

- highly active electrocatalysts for oxygen evolution reaction, *Chemical Engineering Journal*, *Chem. Eng. J.*, 2021, **425**, 131642.
- 51 C. Meng, Y. Cao, Y. Luo, F. Zhang, Q. Kong, A. A. Alshehri, K. A. Alzahrani, T. Li, Q. Liu and X. Sun, A Ni-MOF nanosheet array for efficient oxygen evolution electrocatalysis in alkaline media, *Inorg. Chem. Front.*, 2021, **8**, 3007–3011.
- 52 X. Cai, F. Peng, X. Luo, X. Ye, J. Zhou, X. Lang and M. Shi, Understanding the Evolution of Cobalt-Based Metal–Organic Frameworks in Electrocatalysis for the Oxygen Evolution Reaction, *ChemSusChem*, 2021, **14**, 3163–3173.
- 53 D. Miles, D. Jiang, A. Burrows, J. Halls and F. Marken, Conformal transformation of Conformal transformation of [Co(bdc)(DMF)] (Co-MOF-71, bdc = 1,4-benzenedicarboxylate, DMF = N,N-dimethylformamide) into porous electrochemically active cobalt hydroxide, *Electrochem. Commun.*, 2013, **27**, 9–13.
- 54 L. Aguilera, P. Aguiar, Y. Ruiz, A. Almeida, J. Moreira, R. Passos and L. Pocrifka, Electrochemical synthesis of  $\gamma$ -CoOOH films from  $\alpha$ -Co(OH)<sub>2</sub> with a high electrochemical performance for energy storage device applications, *J. Mater. Sci.: Mater. Electron.*, 2020, **31**, 3084–3091.
- 55 W. Zhou, D. Huang, Y.-P. Wu, J. Zhao, T. Wu, J. Zhang, D.-S. Li, C. Sun, P. Feng and X. Bu, Stable Hierarchical Bimetal–Organic Nanostructures as High Performance Electrocatalysts for the Oxygen Evolution Reaction, *Angew. Chem., Int. Ed.*, 2019, **58**, 4227–4231.
- 56 L. Yaqoob, T. Noor and N. Iqbal, A comprehensive and critical review of the recent progress in electrocatalysts for the ethanol oxidation reaction, *RSC Adv.*, 2021, **11**, 16768.
- 57 D. Yu, Y. Hao, S. Han, S. Zhao, Q. Zhou, C. Kuo, F. Hu, L. Li, H. Chen, J. Ren and S. Peng, Ultrafast Combustion Synthesis of Robust and Efficient Electrocatalysts for High-Current-Density Water Oxidation, *ACS Nano*, 2023, **17**, 1701–1712.